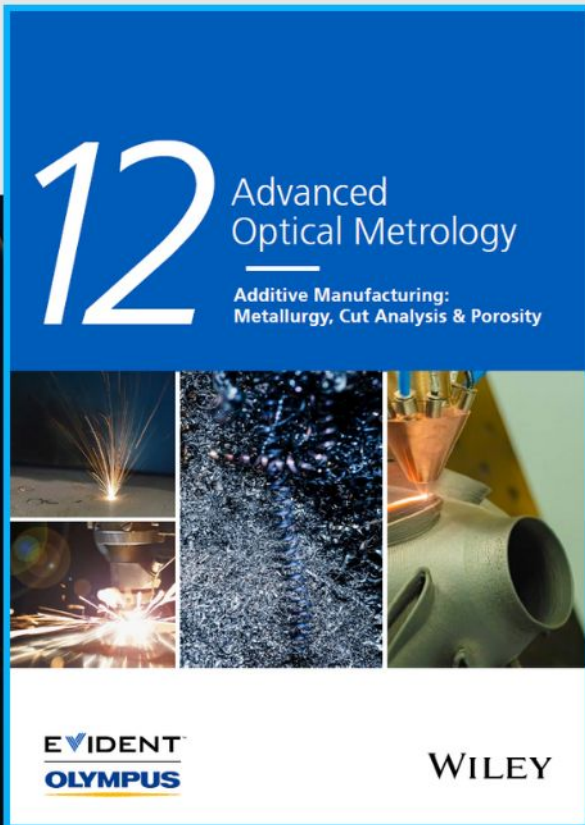




Additive Manufacturing: Metallurgy, Cut Analysis & Porosity



The latest eBook from
Advanced Optical Metrology.
Download for free.

In industry, sector after sector is moving away from conventional production methods to additive manufacturing, a technology that has been recommended for substantial research investment.

Download the latest eBook to read about the applications, trends, opportunities, and challenges around this process, and how it has been adapted to different industrial sectors.

EVIDENT™
OLYMPUS

WILEY

Atomically Smooth Graphene-Based Hybrid Template for the Epitaxial Growth of Organic Semiconductor Crystals

Nguyen Ngan Nguyen, Hyo Chan Lee, Kangkyun Baek, Min Seok Yoo, Hansol Lee, Hyungsub Lim, Shinyoung Choi, Cheol-Joo Kim, SungWoo Nam,* and Kilwon Cho*

Atomically thin 2D materials are good templates to grow organic semiconductor thin films with desirable features. However, the 2D materials typically exhibit surface roughness and spatial charge inhomogeneity due to nonuniform doping, which can affect the uniform assembly of organic thin films on the 2D materials. A hybrid template is presented for preparation of highly crystalline small-molecule organic semiconductor thin film that is fabricated by transferring graphene onto a highly ordered self-assembled monolayer. This hybrid graphene template has low surface roughness and spatially uniform doping, and it yields highly crystalline fullerene thin films with grain sizes >300 nm, which is the largest reported grain size for C₆₀ thin films on 2D materials. A graphene/fullerene/pentacene phototransistor fabricated directly on the hybrid template has five times higher photoresponsivity than a phototransistor fabricated on a conventional graphene template supported by a SiO₂ wafer.

1. Introduction


Organic semiconductors (OSCs) have numerous possible optoelectronic applications, including light-emitting diodes (OLED), field-effect transistors (FETs), photovoltaics, and photodetectors.^[1,2]

Dr. N. N. Nguyen, Dr. M. S. Yoo, Dr. H. Lee, H. Lim, S. Choi,
Prof. C.-J. Kim, Prof. K. Cho
Department of Chemical Engineering
Pohang University of Science and Technology
Pohang 37673, Republic of Korea
E-mail: kwcho@postech.ac.kr

Dr. H. C. Lee
Department of Mechanical Science and Engineering
University of Illinois at Urbana – Champaign
Urbana, IL 61801, USA

Dr. K. Baek
Center for Self-assembly and Complexity (CSC)
Institute for Basic Science (IBS)
Pohang 37673, Republic of Korea

Prof. S. Nam
Department of Mechanical Science and Engineering/Department
of Materials Science and Engineering
University of Illinois at Urbana – Champaign
Urbana, IL 61801, USA
E-mail: swnam@illinois.edu

 The ORCID identification number(s) for the author(s) of this article can be found under <https://doi.org/10.1002/adfm.202008813>.

DOI: 10.1002/adfm.202008813

Optoelectronic devices with novel functionalities have been developed by van der Waals hybridization of OSCs with 2D materials.^[3] These OSC thin films are the active layers of such devices and determine the devices' performances. Consequently, OSC thin films must have the desired molecular orientation, morphology, grain size, and crystallinity.^[2,4]

Modification of substrate surfaces is a common method to obtain high-quality OSC thin films, particularly for films deposited from the vapor phase.^[5] The molecular orientations of OSC thin films are determined by the balance between the intermolecular interactions and the molecule–substrate interactions; when the interactions between the OSC molecules and the substrate change, the molecular orientations of the OSC molecules change accordingly.^[6] One of the most investigated methods to modify

silicon dioxide (SiO₂) dielectric surfaces is to apply alkylsilane molecules. The most typical silane is octadecyltrichlorosilane (ODTS): the Si atoms of ODTS are grafted onto the surface of SiO₂ by siloxane (Si–O–Si) bonds and its long alkyl chains order into well-packed grains to form a self-assembled monolayer (SAM). Substrates modified with ODTS-SAM have ultrasmooth and hydrophobic surfaces that enable the growth of high-quality thin films of small-molecule OSCs such as pentacene and fullerene (C₆₀).^[7,8] Furthermore, the phase state (i.e., ordered or disordered) of the ODTS-SAM influences the properties of the resulting OSC thin films.^[8] On ordered ODTS-SAM (o-ODTS-SAM), pentacene thin films contain smaller grains than on disordered ODTS-SAM (d-ODTS-SAM). However, the o-ODTS-SAM and pentacene have a quasi-epitaxial relationship, so pentacene grains on o-ODTS-SAM have higher crystallinity, and hence higher charge carrier mobilities, than on d-ODTS-SAM.

Graphene has been evaluated as a good template for OSC growth because the growth of OSC thin films on graphene is highly controllable, especially by modulating its Fermi level E_F .^[9,10] The E_F of graphene determines how the OSC molecules and graphene interact, and thus influences the molecular arrangement and nucleation dynamics of the OSC molecules. As a result, graphene templates are effective tools for fabrication of OSC/graphene hybrid materials with atomically clean interfaces.

However, charged impurities usually occur at the interface between the SiO₂ substrate and graphene; they induce charge fluctuations in the graphene basal plane and dope the graphene.^[11] Furthermore, the graphene layer coats the underlying

substrate conformally, so the substrate's roughness is transferred to the graphene template, and OSC thin films that develop on such graphene/substrate system have low crystallinity.

In this study, we addressed these problems by investigating the growth behaviors of C_{60} on graphene hybrid templates (graphene/ODTS-SAM). When an ODTS-SAM was inserted between graphene and the substrate, the corrugation of graphene was suppressed and the amplitude of electron-hole puddles in graphene was significantly reduced. Consequently, C_{60} thin films had higher crystallinity when grown on the graphene/ODTS-SAM hybrid templates than when grown on graphene templates that did not have an ODTS-SAM. Graphene yielded a larger grain size and a larger average crystallite size in the grains of C_{60} on an o-ODTS-SAM than on a d-ODTS-SAM. Phototransistors fabricated by sequential deposition of C_{60} and pentacene directly on graphene templates had five times greater visible-range photoresponsivity when an o-ODTS-SAM was used than when a bare SiO_2 substrate was used.

2. Results and Discussion

2.1. Nucleation and Growth of C_{60} Thin Film on Graphene-Based Hybrid Templates

First, we prepared bare SiO_2/Si substrates and ODTS-SAM-treated SiO_2/Si substrates. ODTS-SAM was grafted onto the SiO_2 substrates by dipping cleaned SiO_2 into ODTS solutions at either -20 or 30 °C. At -20 °C, a highly o-ODTS-SAM formed (Figure 1a, left and Figure 1b). But at 30 °C, the reaction between the ODTS molecules and the SiO_2 substrate was rapid

so that the density of the ODTS-SAM molecules significantly decreased;^[8] this reduction in the molecular density prevents the close packing of the ODTS-SAM, so a d-ODTS-SAM formed (Figure 1a, right). We then transferred graphene onto the o-ODTS or d-ODTS-SAM to prepare graphene/o-ODTS-SAM and graphene/d-ODTS-SAM hybrid templates.

These hybrid templates have distinct differences, as can be identified using 2D grazing incidence X-ray diffraction (GIXD, Figure 1c). The graphene/o-ODTS-SAM template showed a clear peak near $(q_{xy}, q_z) = (1.48 \text{ \AA}^{-1}, 0)$, which corresponds to a monolayer (ML) hexagonal lattice structure with an intermolecular distance of 4.87 \AA (Figure 1b). In contrast, the graphene/d-ODTS-SAM did not show this peak; this absence implies that the alkyl chains are amorphous. Despite this difference in ordering, the mechanical strain did not differ between graphene on o-ODTS-SAM and graphene on d-ODTS-SAM (Figures S1, S2, Supporting Information). Graphene/o-ODTS-SAM and graphene/d-ODTS-SAM were similarly hydrophobic, whereas graphene/ SiO_2 was hydrophilic (Figure S3, Supporting Information).

The roughness of both graphene templates was measured by using tapping-mode atomic force microscopy (AFM) (Figure S4, Supporting Information). In both graphene/ODTS-SAM cases, the root-mean-square roughness R_{RMS} was much less than that of the graphene/ SiO_2 template (Figure 1d; Figure S4, Supporting Information). Furthermore, graphene/o-ODTS-SAM was slightly less rough than graphene/d-ODTS-SAM.

Although the tapping-mode AFM results suggest that the surface roughnesses of graphene/o-ODTS-SAM and graphene/d-ODTS are almost the same, these results do not take into account the rapid movement of the alkyl chains of the d-ODTS-SAM, because tapping-mode AFM only measures

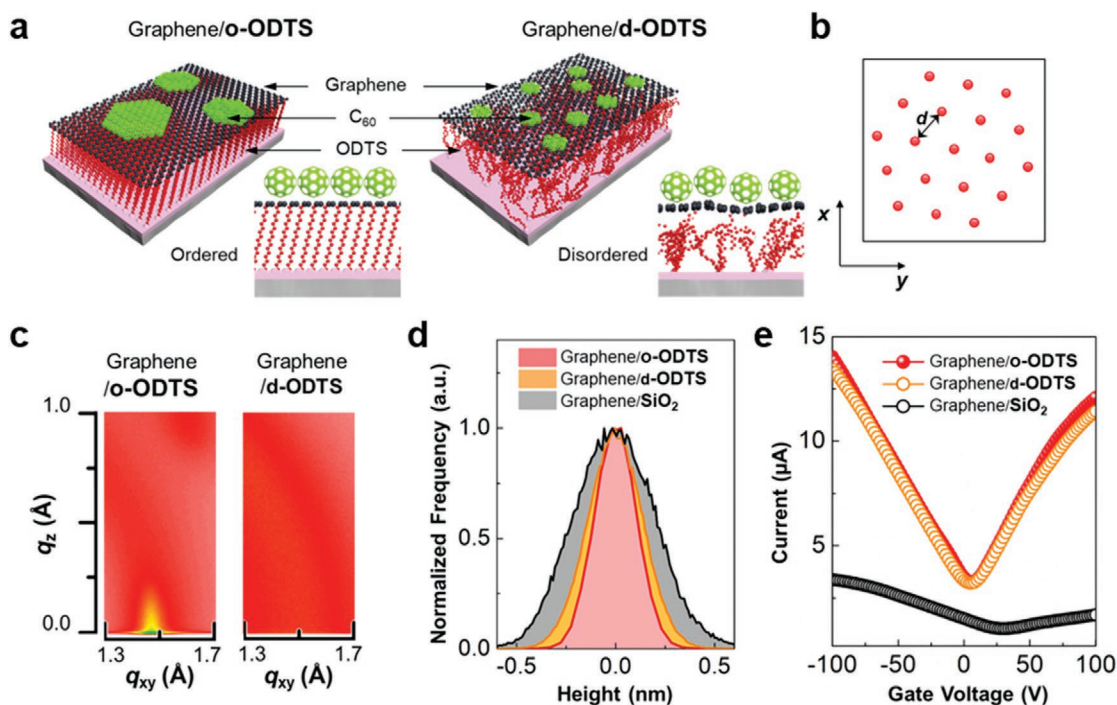


Figure 1. Properties of graphene hybrid templates. a) Scheme of hybrid templates. b) Top schematic view of ODTS-SAM. c) GIXD patterns of hybrid templates. d) Normalized height histograms of hybrid templates and graphene. e) Transfer curves of graphene-FET with and without ODTS-SAM.

the time-averaged interactions between the tip and the surface. According to a recent molecular dynamics simulation,^[12] a closely packed ODTS-SAM has a surface roughness of 2.1 Å but the roughness increases to 4.1 Å when the packing density is halved. In addition, for d-ODTS-SAM, the period of corrugation has been estimated to be ≈5 nm, so graphene is expected to conformally coat the d-ODTS-SAM.^[13] Thus the actual roughness of the graphene/d-ODTS-SAM template is expected to be higher than that of the graphene/o-ODTS-SAM template.

As discussed above, the presence of the ODTS-SAM between the graphene layer and the SiO₂ substrate reduces the degree of electron–hole puddles. This effect strongly alters the charge-transport behaviors of graphene FETs (Figure 1e). For instance, graphene on a bare SiO₂ substrate was p-type doped, whereas graphene FETs on ODTS-SAMs exhibited near-zero doping, as was evident in the left shift in the Dirac voltage V_D . In addition, the charge carrier mobility μ of graphene FETs was estimated by using a constant-mobility model^[14]

$$R = \frac{(L/W)}{\mu e \sqrt{n_{\text{res}}^2 + (\alpha(V_G - V_D))^2}} \quad (1)$$

where L is the channel length, W is the channel width, e is the elementary charge, n_{res} is the residual carrier density at $V_G = V_D$, and α is $7.2 \times 10^{10} \text{ cm}^{-2}$. A graphene FET fabricated on bare SiO₂ substrate had $\mu \approx 1800 \text{ cm}^2 \text{ V}^{-1} \cdot \text{s}^{-1}$ and $n_{\text{res}} \approx 1.8 \times 10^{12} \text{ cm}^{-2}$. In contrast, the graphene FETs fabricated on the ODTS-SAM substrates had $\mu \approx 6000 \text{ cm}^2 \text{ V}^{-1} \cdot \text{s}^{-1}$ and $n_{\text{res}} \approx 1.1 \times 10^{12} \text{ cm}^{-2}$. The increase in the μ and the decrease in the n_{res} of graphene FETs prepared with an ODTS-SAM indicate that its long alkyl chains effectively separate graphene from the charged impurities on the SiO₂ surface, and thus reduce the amplitude of electron–hole puddles in graphene.^[11] However, the effects of the phase state of ODTS on the electron–hole puddles of graphene FET are negligible because both o-ODTS and d-ODTS-SAM provide a sufficient physical gap between graphene and the SiO₂ surface.

O-ODTS-SAM effectively reduces the roughness of the graphene surface and the amplitude of electron–hole puddles. However, similar effects can also be achieved by inserting hexagonal boron nitride (hBN) between graphene and the SiO₂ substrate.^[11] So the effectiveness in hybrid templates of o-ODTS-SAM and hBN must be compared. First, modification of SiO₂ wafers by using ODTS-SAMs is a standard, low cost, and reliable process used in organic electronics, whereas the synthesis of uniform hBN on the wafer scale and its transfer to SiO₂ substrates are very challenging. Moreover, the insertion of wafer-scale hBN between graphene and a SiO₂ substrate increases the μ of graphene by at most a factor of 3.^[15] In contrast, we confirmed in this study that dry-transferring graphene onto o-ODTS-SAM increased the μ of graphene by a factor of 3.3, and graphene on o-ODTS-SAM had higher μ than graphene on hBN that had been produced using chemical vapor deposition (CVD) (Figure S5, Supporting Information). These results, combined with the scalability of the process, suggest that o-ODTS-SAM is better than CVD-grown hBN as a substrate in graphene FETs.

The effects of the hybrid graphene templates and the graphene/SiO₂ template on the growth of OSCs were then investigated by

using C₆₀ as a model compound. During C₆₀ deposition, we applied a gate voltage at the Dirac point of each graphene layer to eliminate the effects of graphene doping on the growth dynamics of the C₆₀ ad-molecules (Figure 2a). Note that the Dirac points of graphene on ODTS-SAMs were close to 0 V, so this application of gate voltages had negligible effect on the growth behaviors of C₆₀ on the hybrid graphene/ODTS templates.

AFM images of the C₆₀ thin films grown on the templates were obtained (Figure 2b,c; Figure S6, Supporting Information). In the early stages of C₆₀ thin film growth, when the nominal thickness was 0.75 ML, the nucleation density and the average of height of C₆₀ depended strongly on the templates. The use of the hybrid graphene/o-ODTS-SAM template yielded a reduction in nucleation density and a consequent increase in grain size. The average nucleation density of C₆₀ was much less on the graphene/o-ODTS-SAM template ($9 \mu\text{m}^{-2}$) than on the graphene/d-ODTS-SAM template ($88 \mu\text{m}^{-2}$) and the graphene/SiO₂ template ($143 \mu\text{m}^{-2}$). The grain size of C₆₀ was ≈300 nm on the graphene/o-ODTS-SAM template (Figure 2c); this is the largest reported grain size for C₆₀ deposited on 2D materials.^[9]

Given that the nucleation density is inversely proportional to the diffusivity of ad-molecules on the surface, these results imply that the surface diffusion of C₆₀ ad-molecules is much more rapid when the graphene/o-ODTS-SAM template is used. Moreover, most nucleation islands were 0.8 nm high, which corresponds to the diameter of a single C₆₀ molecule (Figure 2b). This result implies that only monolayers of C₆₀ molecules form on the hybrid templates. In contrast, the average height of C₆₀ islands on the graphene/SiO₂ substrate was 6 nm, which indicates that vertical growth of the C₆₀ thin film dominates lateral growth in this case.

Interestingly, this trend is opposite to what was reported for the growth of OSCs on ODTS-SAMs in the absence of graphene.^[8] The growth of OSCs on d-ODTS-SAM without graphene on top has been found to produce OSC grains with larger sizes than growth on o-ODTS-SAM. In this case, the mobile alkyl chains of the loosely packed ODTS-SAM might assist the diffusion of the OSC ad-molecules, and thereby yield increase in the grain size of the resulting OSC thin film.

During the final growth stage (10 ML), the surfaces of all the templates were mostly covered by the C₆₀ thin films (Figure 2d). However, distinct differences occurred: on the graphene/o-ODTS-SAM template, a uniform C₆₀ thin film with pancake-like grains covered the whole surface, whereas on the graphene/d-ODTS-SAM template, empty trenches were present between large C₆₀ grains. Similarly, only small C₆₀ crystallites were present on the surface of graphene/SiO₂, with empty areas between them. As a result, the R_{RMS} of C₆₀ deposited on graphene/o-ODTS-SAM template was very low (≈1 nm) compared to that on graphene/d-ODTS-SAM (≈3 nm) and on the graphene/SiO₂ template (≈7 nm).

We also observed the growth of C₆₀ thin film on graphene/CVD hBN hybrid template. (Figure S7, Supporting Information). The graphene/CVD hBN hybrid template caused vertical growth of C₆₀ thin film, so it was nonuniform. This result is further evidence that the o-ODTS-SAM is better than CVD hBN as a large-area substrate for graphene-based hybrid templates.

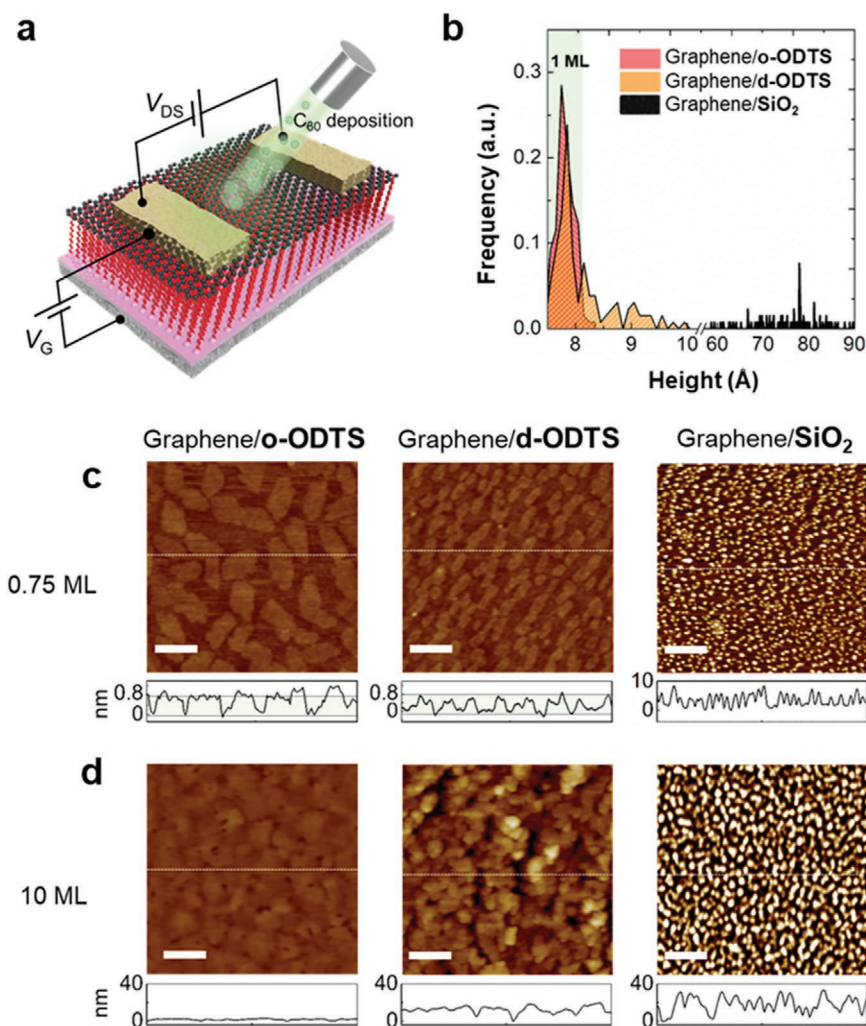


Figure 2. Growth evolution of C_{60} on hybrid templates and graphene/ SiO_2 . a) Scheme of fabrication system of C_{60} layer on graphene hybrid templates. b) Height histogram of C_{60} on different hybrid templates at 0.25 ML thickness. AFM images of C_{60} crystals on different hybrid templates at c,d) deposition doses were 0.75 and 10 ML, respectively. Scale bar: 400 nm.

2.2. Crystallinity of C_{60} Thin Film Grown on Graphene-Based Hybrid Templates

We now focus on the arrangement of C_{60} molecules on each template. A submonolayer of C_{60} grown on each template was characterized using low-voltage high resolution transmission electron microscopy (HR-TEM) and GIXD. On graphene/o-ODTS-SAM and graphene/d-ODTS-SAM, the C_{60} grains with exact single-molecule-thickness exhibited hexagonal arrangement that corresponds to a $C_{60}(111)$ monolayer with the fcc structure (Figure 3a). This molecular arrangement implies that the C_{60} and graphene layers have an epitaxial relationship.^[9,16,17]

The C_{60} layer prepared on the graphene/d-ODTS-SAM hybrid template showed defective regions (e.g., amorphous areas, twin domains, point defects), whereas the layer prepared with the graphene/o-ODTS hybrid template did not have them (Figure 3b). In contrast, the C_{60} layer grown on the graphene/ SiO_2 template exhibited a multilayer structure rather than a

$C_{60}(111)$ monolayer (Figure 3c); this result is consistent with the AFM observation that C_{60} grains grown on the graphene/ SiO_2 template were present in a vertically stacked molecular layer even when the deposition dose was sub-ML (Figure 2b). Apart from the predominant ABC stacking of the $C_{60}(111)$ layers, defective features such as grain boundaries and tilted domains were abundant on the graphene/ SiO_2 template. Further, the structure of the top layer was considerably disordered over a large areal fraction of the imaged regions on this graphene/ SiO_2 template (Figure S8, Supporting Information).

To investigate the molecular assembly of C_{60} on graphene on the scale of a few hundred nanometers (>500 nm, which is the electron-beam size), the same HR-TEM samples were characterized using selected-area electron diffraction (SAED) (Figure 3a–c, lower). In all cases, hexagonal diffraction patterns due to $C_{60}(111)$ were observed inside a single set of graphene hexagonal patterns; this observation implies that the C_{60} patterns were due to domains on a single grain of graphene. The SAED patterns of C_{60} and those of graphene feature misorientation angles of

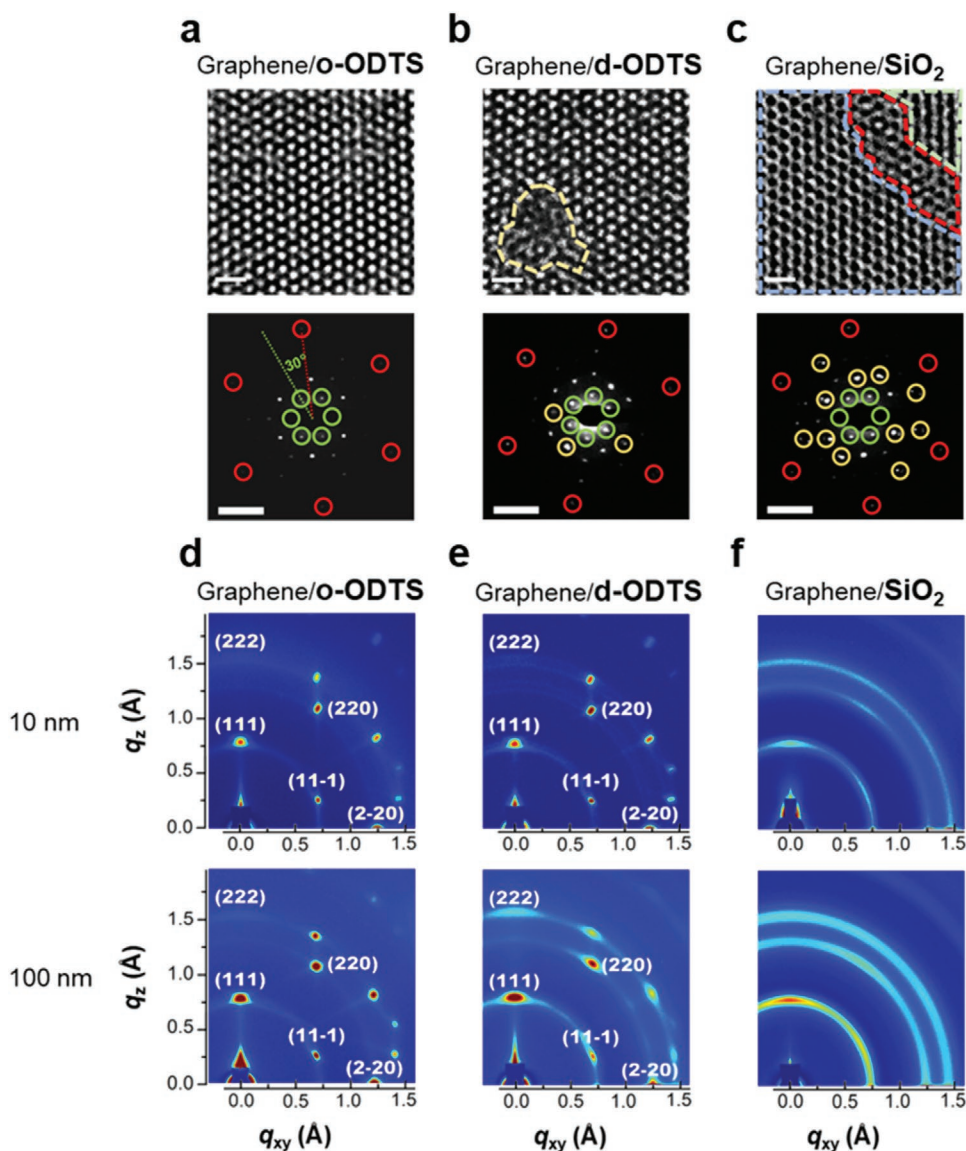


Figure 3. Molecular arrangement and crystal structure of C_{60} on hybrid template. HR-TEM images and the corresponding SAED patterns of monolayers C_{60} grown on a) graphene/o-ODTS-SAM, b) graphene/d-ODTS-SAM and c) graphene/ SiO_2 . In SAED patterns, red, green, and yellow circles mark patterns of graphene, C_{60} domain and C_{60} multidomain respectively. Scale bars in TEM images and in SAED patterns are 2 nm and 2 nm^{-1} , respectively. GIXD patterns of intermediate and bulk thickness of C_{60} layers grown on d) graphene/o-ODTS-SAM, e) graphene/d-ODTS-SAM, and f) graphene/ SiO_2 .

$\approx 0^\circ$ or $\approx 30^\circ$, which are energetically stable arrangements of C_{60} molecules along the armchair and zigzag directions of graphene respectively.^[17] This result confirms the epitaxial relationship between the lowermost C_{60} layer and graphene.

The substrate affected the uniformity of the C_{60} layer. The layer prepared on the graphene/o-ODTS-SAM hybrid template showed only a single set of C_{60} diffraction patterns for each set of graphene diffraction patterns; this result suggests that the single-crystalline C_{60} monolayer was extremely large ($>500\text{ nm}$) (Figure 3a). In contrast, the C_{60} layer was not uniform on either the graphene/d-ODTS-SAM hybrid template (Figure 3b) or the graphene/ SiO_2 template (Figure 3c). On those templates, each set of graphene diffraction patterns showed several sets of C_{60} diffraction patterns; this result implies that many small C_{60} domains were present within each

graphene grain. These features are in good agreement with our AFM results (Figure 2).

The effects of the graphene hybrid templates on the crystal structures of the C_{60} thin films over a macroarea were also examined using GIXD. At the nominal thickness of 10 nm (Figure 3d–f, upper), a set of reflections belonging to the (111) family was observed for the C_{60} thin films on all the templates. However, the diffraction spots for the C_{60} thin film prepared on the graphene/o-ODTS-SAM hybrid template (Figure 3d) were sharper than those for the C_{60} thin films prepared on the other templates (Figure 3e,f). In addition, the intensity of the ring patterns, which reveals the proportion of randomly oriented crystals in the C_{60} film, was significantly high in the GIXD patterns of the graphene/ SiO_2 template. These differences became increasingly pronounced as the thickness of the

C_{60} films increased (Figure 3d–f, lower). The GIXD pattern of 100 nm thick C_{60} films grown on the graphene/o-ODTS-SAM hybrid template had $C_{60}(111)$ single-crystalline features (Figure 3d). The GIXD pattern for the 100 nm thick C_{60} film grown on the graphene/d-ODTS-SAM hybrid template showed strong $C_{60}(111)$ diffraction patterns, but the spots were broader than those of the 10 nm thick C_{60} film grown on the same template, and ring patterns were also clearly evident (Figure 3e). The GIXD pattern for the C_{60} film grown on the graphene/ SiO_2 template had completely amorphous characteristics (Figure 3f), i.e., the upper layers of the C_{60} film merely consisted of randomly oriented nanocrystals.

In our previous study of highly crystalline C_{60} thin films grown on graphene templates, we found that the electrical gating of the graphene template with a large negative gate bias during C_{60} deposition was required for the suppression of electron transfer from graphene to C_{60} , so that the Coulombic repulsive interactions between C_{60} ad-molecules could be minimized.^[9] However, the insertion of an o-ODTS-SAM between graphene and the SiO_2 substrate eliminates the need for in situ electrical gating during preparation of highly crystalline C_{60} thin films; this result occurs because the o-ODTS-SAM reduces the surface roughness of the graphene template and leaves nearly negligible charge puddles, so the grain size and crystallinity of the C_{60} thin film grown on the graphene/o-ODTS-SAM template are comparable with those of the C_{60} thin film grown on the graphene/ SiO_2 template with in situ electrical gating.

2.3. Growth Mechanism of C_{60} Thin Film on Graphene-Based Hybrid Templates

To determine the effects of graphene roughness on the growth behaviors of the C_{60} thin films, density functional theory (DFT) calculations were conducted for a C_{60} ad-molecule on a graphene substrate (Figure 4, see also the Experimental Section). In these calculations, we only considered the most common configuration in which a hexagonal side of the C_{60} molecule faces the graphene surface.^[16,17] First, the adsorption energies E_{ads} of a C_{60} molecule on flat graphene were calculated for the configurations in which a hexagonal side of C_{60} and graphene form AB-stacking (Figure 4a, left) or AA-stacking (Figure 4a, right). The equilibrium distance between graphene and the center of mass of C_{60} was estimated to be 6.53 Å (Figure S9, Supporting Information), which is very close to the previously reported value.^[18] The AB-stacked C_{60} molecule had $E_{ads} = 0.65$ eV and the AA-stacked C_{60} molecule had $E_{ads} = 0.62$ eV. The small difference between E_{ads} in these two different positions implies that the diffusion barrier E_D of the C_{60} ad-molecule on flat graphene is negligible (Figure 4c). However, when the calculation included sub-nanoscale roughness of graphene, E_{ads} varied significantly. On a concave surface, the C_{60} molecule had $E_{ads} = 0.84$ eV as a result of the increased effective contact area between C_{60} and graphene (Figure 4b, left), whereas on a convex surface, the C_{60} molecule had $E_{ads} = 0.49$ eV (Figure 4b, right). Thus, sub-nanoscale corrugation of graphene increases the E_D of the C_{60} ad-molecule in our model system to ≈ 0.15 eV, which is larger than thermal energy at room temperature ($k_B T = 0.025$ eV) (Figure 4c). In all cases, E_{ads} is much higher than the thermal

energy at room temperature, so C_{60} molecules rarely desorb from the graphene surface.

When the desorption of ad-molecules is inhibited and if we assume the critical nucleus size is 1 as the literature, the nucleation density of the film is proportional to $\exp\left(\frac{E_D}{2k_B T}\right)$, where $k_B T$ is the thermal energy.^[19] At room temperature, the 0.15 eV increase in E_D due to sub-nanoscale corrugation of graphene results in an increase in the nucleation density by a factor of 20, which is of the same order as the observed nucleation density difference between C_{60} on the graphene/o-ODTS-SAM template and C_{60} on the graphene/d-ODTS-SAM or graphene/ SiO_2 templates (Figure 2).

Electron–hole puddles in graphene also limit the diffusion of C_{60} ad-molecules on the graphene surface. Charge transfer between graphene and C_{60} molecules is determined by the Fermi level of graphene, so the presence of electron–hole puddles means that the charged states of the C_{60} ad-molecules vary with their location. As a result, the potential energies of the C_{60} ad-molecules fluctuate because E_{ads} of C_{60} on graphene is affected by C_{60} 's charged state. Therefore, the diffusivity of C_{60} ad-molecules should be lowest on the graphene/ SiO_2 template for which the surface roughness and the amplitude of the electron–hole puddles are highest. This prediction is consistent with our experimental observation that the graphene/ SiO_2 template yielded C_{60} thin films with a small grain size and a large nucleation density.

The crystallinity and growth behaviors of C_{60} thin films differed among on the three templates (Figure 4d). These results can be attributed to the variation in the surface roughness of the graphene templates, because a corrugated graphene surface impedes formation of highly crystalline OSC monolayers.^[20] The growth mode and crystallinity of the C_{60} thin films in the early stages of growth are critically affected by the arrangement of the C_{60} molecules within the first ML near the graphene template. On a C_{60} layer with negligibly small imperfections, the diffusion barrier and the Ehrlich–Schwoebel barrier to the motions of C_{60} ad-molecules are sufficiently small to induce the layer-by-layer growth of C_{60} thin films.^[21] However, on defective C_{60} nuclei, which were found on graphene/ SiO_2 , the surface diffusion of C_{60} ad-molecules is hampered, so the ad-molecules are prevented from reaching the edge of the nuclei. As a result, the lateral growth of C_{60} is expected to be limited and the C_{60} nuclei will grow vertically. Moreover, the C_{60} nuclei formed on an amorphous C_{60} layer are randomly oriented or amorphous due to the lack of epitaxy in this case. As a result, subsequent C_{60} layers that form on the low-crystallinity C_{60} layer include various lattice orientations or amorphous regions.

2.4. Graphene–Organic Semiconductor Heterojunction Phototransistors

To demonstrate the usefulness of our graphene hybrid templates in optoelectronic applications, we fabricated graphene–OSC heterojunction phototransistors by using graphene hybrid templates and graphene/ SiO_2 . We also compared the efficiencies of the graphene–OSC phototransistors fabricated on

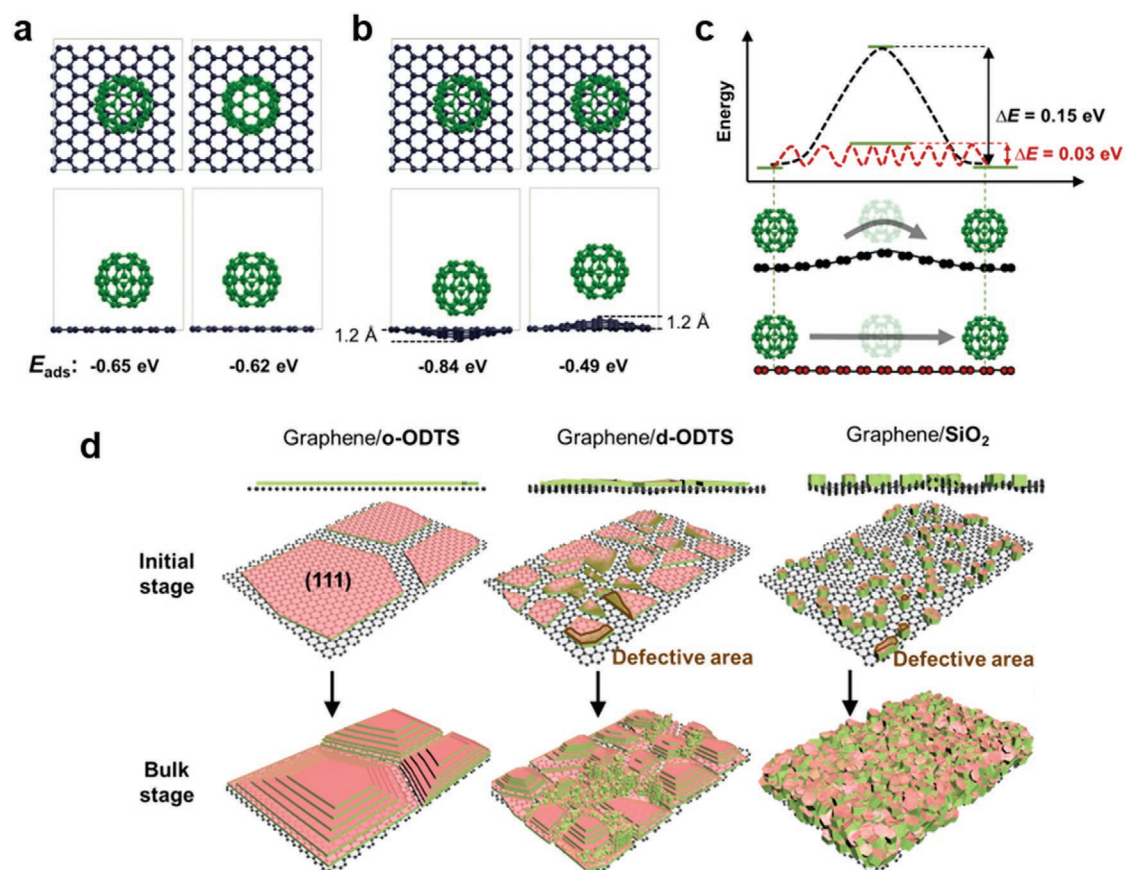


Figure 4. Mechanism of C_{60} grown on hybrid and graphene templates. DFT calculation of C_{60} adsorption energy on a) extremely flat graphene and b) graphene with curvatures. c) Diffusion of C_{60} on extremely flat graphene and graphene with curvatures. d) Schematic growth mechanism of C_{60} on hybrid templates and graphene.

the three different templates (Figure 5; Figures S10 and S11, Supporting Information). To fabricate the devices, we first deposited source/drain electrodes on the templates. On each template, a 10 nm C_{60} thin film and a 20 nm pentacene thin film were sequentially deposited using an organic molecular beam deposition system (OMBD, Figure 5a). A C_{60} thin film has lowest unoccupied molecular orbital (LUMO) = -4.5 eV and highest unoccupied molecular orbital (HOMO) = -6.5 eV, and a pentacene thin film has LUMO = -2.9 eV and HOMO = -5.1 eV. Because of the differences between corresponding orbital levels, the C_{60} and pentacene thin films form a type-II heterojunction when in contact (Figure 5a, right). Under illumination with visible light, this built-in electric field promotes separation of electrons and holes that are generated inside C_{60} and pentacene thin films so that holes accumulate in the pentacene thin films and electrons are transferred from C_{60} to graphene. As a consequence of this efficient charge separation, significant electron doping in graphene can occur and thus a large responsivity can be generated. The Dirac voltage of the graphene transistor shifted toward 0 V under visible light illumination (430–680 nm) (Figure 5b); this change demonstrates the n-type doping of initially p-doped graphene due to the photogating effect.

For comparison, we fabricated similar devices on graphene/d-ODTS-SAM and graphene/ SiO_2 templates (Figure S10,

Supporting Information). For all devices, the response time was <300 ms, which is the temporal resolution of the measurement (Figure 5c). However, the devices' photoresponsivities depended strongly on the underlying templates (Figure 5d). Under illumination with visible light, the photoresponsivity is highest for the device fabricated by using the graphene/o-ODTS-SAM template and lowest for that fabricated by using the graphene/ SiO_2 template. At a wavelength of 430 nm, the photoresponsivities were 2010 A W^{-1} in device fabricated using graphene/o-ODTS-SAM, 777 A W^{-1} in that fabricated using graphene/d-ODTS-SAM, and 430 A W^{-1} in that fabricated using graphene/ SiO_2 templates.

We calculated the internal photoresponsivities of the devices under illumination with visible light by normalizing the photoresponsivity data to the absorbance of the devices, to accurately compare them after accounting for the absorption differences (Figure S11, Supporting Information). Compared to the phototransistor fabricated by using the graphene/ SiO_2 template, the normalized photoresponsivity was increased by a factor of 5 when the phototransistor was fabricated by using the graphene/o-ODTS-SAM template.

We also compared the photocurrent I_P to dark current I_D ratio I_P/I_D of the devices (Figure S12, Supporting Information). The phototransistor fabricated using the graphene/o-ODTS-SAM template had the highest I_P/I_D .

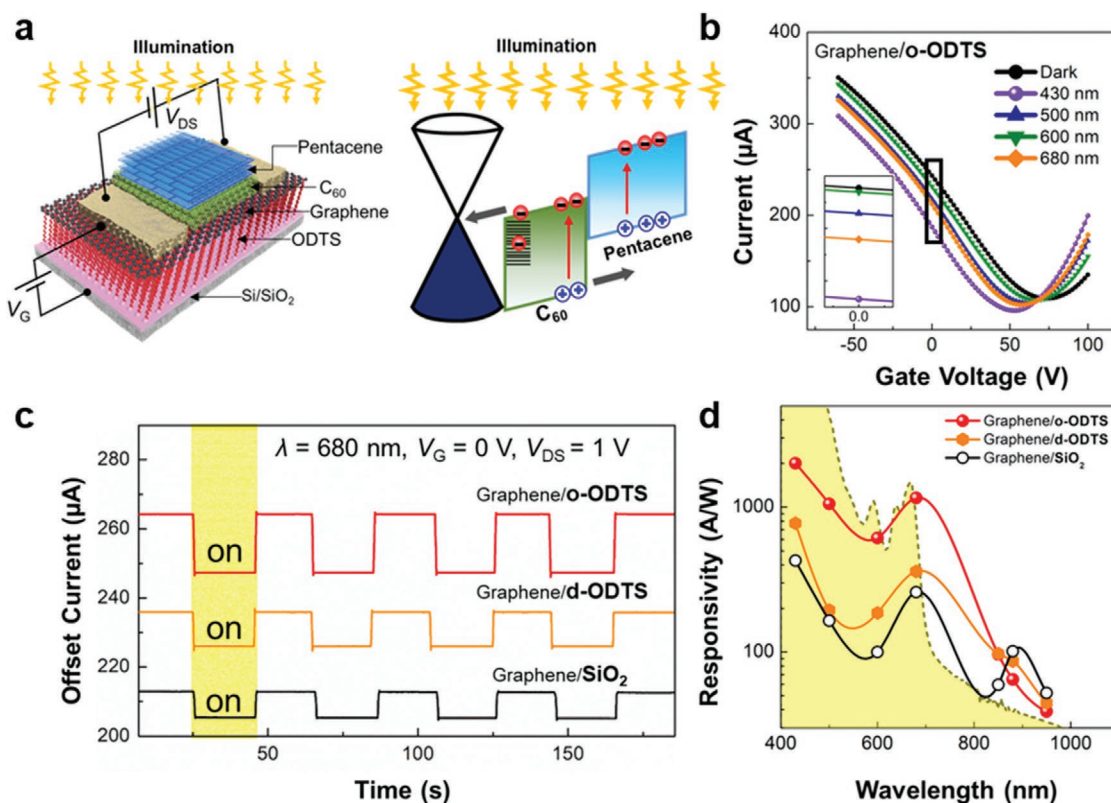


Figure 5. Performance of C₆₀-pentacene phototransistors with and without hybrid templates. a) Scheme of device and working principles. b) Transfer curve of phototransistors with graphene/o-ODTS-SAM template. Inset: transfer curves at V_G ≈ 0. c) Offset channel current versus time. d) Photoresponsivity of phototransistors with and without hybrid templates. Shaded area: optical absorption spectrum of photoactive layer.

To determine why the device fabricated by using the graphene/o-ODTS-SAM template had increased photoresponsivity under visible light, we investigated the morphology of the pentacene thin film in the phototransistor fabricated on each template (Figure S13, Supporting Information). The pentacene grain size was largest when deposited on the C₆₀/graphene/o-ODTS-SAM, probably because of the high crystallinity and low roughness of its C₆₀ film. In addition, the pentacene molecules laid flat in the device fabricated using the graphene/ODTS hybrid templates, whereas a large number of pentacene crystallites were in the standing up orientation in the device fabricated by using the graphene/SiO₂ template. The enlarged grain size with high crystallinity and the flat-lying orientation of the pentacene thin film in the device fabricated using the graphene/o-ODTS-SAM template increase the vertical diffusion length of excitons in the pentacene thin film.^[10,22] The diffusion length of excitons in the C₆₀ thin film will also be largest for the graphene/o-ODTS-SAM template because of the high crystallinity of the resulting C₆₀ thin film. This increased exciton diffusion length increases the number of excitons that reach the C₆₀/pentacene and graphene/C₆₀ interfaces, and thus increases the numbers of electrons and holes that can be separated at the interface; as a result, photocurrent is high.

3. Conclusion

We have developed new types of hybrid templates that are composed of graphene and an ODTS-SAM. These templates can be used to prepare high-quality OSC thin films. We have also carefully investigated the effects of the graphene/ODTS-SAM hybrid templates on the growth behaviors of C₆₀ thin films on graphene. The ODTS-SAM facilitates lateral growth of highly crystalline C₆₀ thin films and enlarges the average grain size by flattening the graphene's surface and reducing the amplitude of electron-hole puddles in the graphene. A graphene template on highly ordered ODTS-SAM yielded C₆₀ thin films that had a higher crystallinity than the graphene template on the disordered ODTS-SAM. DFT calculations show that the sub-nanometer scale roughness of graphene determines the diffusivity of C₆₀ ad-molecules on its surface, and thus determines the nucleation density and grain size of the resulting C₆₀ thin films. We fabricated graphene phototransistors directly on the graphene/o-ODTS-SAM template by depositing C₆₀ and pentacene thin films in sequence. The clean graphene/C₆₀ interface and the high crystallinity of the resulting OSCs thin films resulted in graphene phototransistors that had high photoresponsivity in the visible range. We believe that our findings advance the technology for fabrication of OSC thin films on graphene templates, and provide

insight into how the properties of the interface between graphene and its substrate affect the formation of highly crystalline OSC thin films.

Supporting Information

Supporting Information is available from the Wiley Online Library or from the author.

Acknowledgements

N.N.N. and H.C.L. contributed equally to this work. This work was supported by the National Research Foundation of Korea (NRF) grants (2020R1A2C3004477) funded by the ministry of Science and ICT, Korea and a grant (Code No.2011-0031628) from the Center for Advanced Soft Electronics under the Global Frontier Research Program of the Ministry of Science and ICT, Korea. S.N. acknowledges support from National Science Foundation (MRSEC DMR-1720633, ECCS-1935775, CMMI-1554019) and Korea Research Institute of Chemical Technology (GO!KRICT KK1963-807). The Pohang Accelerator Laboratory is thanked for providing the synchrotron radiation sources at 3C and 9A beamlines used in this study.

Conflict of Interest

The authors declare no conflict of interest.

Keywords

C₆₀, graphene, growth templates, organic optoelectronics, organic semiconductors

Received: November 6, 2020

Revised: November 28, 2020

Published online: December 21, 2020

- [1] H. Sirringhaus, *Adv. Mater.* **2014**, *26*, 1319.
- [2] H. Dong, X. Fu, J. Liu, Z. Wang, W. Hu, *Adv. Mater.* **2013**, *25*, 6158.
- [3] a) H. Yang, J. Heo, S. Park, H. J. Song, D. H. Seo, K. E. Byun, P. Kim, I. Yoo, H. J. Chung, K. Kim, *Science* **2012**, *336*, 1140; b) W. H. Lee, J. Park, S. H. Sim, S. Lim, K. S. Kim, B. H. Hong, K. Cho, *J. Am. Chem. Soc.* **2011**, *133*, 4447; c) Y. Song, X. Li, C. Mackin, X. Zhang, W. Fang, T. Palacios, H. Zhu, J. Kong, *Nano Lett.* **2015**, *15*, 2104; d) F. H. L. Koppens, T. Mueller, P. Avouris, A. C. Ferrari, M. S. Vitiello, M. Polini, *Nat. Nanotechnol.* **2014**, *9*, 780; e) T.-H. Han, Y. Lee, M.-R. Choi, S.-H. Woo, S.-H. Bae, B. H. Hong, J.-H. Ahn, T.-W. Lee, *Nat. Photonics* **2012**, *6*, 105; f) S. Choi, N. N. Nguyen, Y. Lee, S.-J. Yang, K. Kim, K. Cho, C.-J. Kim, *Adv. Mater. Interfaces* **2020**, *7*, 2000522.
- [4] a) T. Schuettfort, B. Watts, L. Thomsen, M. Lee, H. Sirringhaus, C. R. McNeill, *ACS Nano* **2012**, *6*, 1849; b) D. Khim, A. Luzio, G. E. Bonacchini, G. Pace, M.-J. Lee, Y.-Y. Noh, M. Caironi, *Adv. Mater.* **2018**, *30*, 1705463; c) J. Soeda, T. Okamoto, A. Hamaguchi, Y. Ikeda, H. Sato, A. Yamano, J. Takeya, *Org. Electron.* **2013**, *14*, 1211; d) J. A. Lim, W. H. Lee, H. S. Lee, J. H. Lee, Y. D. Park, K. Cho, *Adv. Funct. Mater.* **2008**, *18*, 229.
- [5] a) H. Ma, H.-L. Yip, F. Huang, A. K. Y. Jen, *Adv. Funct. Mater.* **2010**, *20*, 1371; b) E. Orgiu, P. Samori, *Adv. Mater.* **2014**, *26*, 1827.
- [6] a) R. Ruiz, D. Choudhary, B. Nickel, T. Toccoli, K.-C. Chang, A. C. Mayer, P. Clancy, J. M. Blakely, R. L. Headrick, S. Iannotta, G. G. Malliaras, *Chem. Mater.* **2004**, *16*, 4497; b) D. H. Kim, Y. D. Park, Y. Jang, H. Yang, Y. H. Kim, J. I. Han, D. G. Moon, S. Park, T. Chang, C. Chang, M. Joo, C. Y. Ryu, K. Cho, *Adv. Funct. Mater.* **2005**, *15*, 77.
- [7] a) S. Casalini, C. A. Bortolotti, F. Leonardi, F. Biscarini, *Chem. Soc. Rev.* **2017**, *46*, 40; b) W. H. Lee, J. H. Cho, K. Cho, *J. Mater. Chem.* **2010**, *20*, 2549.
- [8] H. S. Lee, D. H. Kim, J. H. Cho, M. Hwang, Y. Jang, K. Cho, *J. Am. Chem. Soc.* **2008**, *130*, 10556.
- [9] N. N. Nguyen, H. C. Lee, M. S. Yoo, E. Lee, H. Lee, S. B. Lee, K. Cho, *Adv. Sci.* **2020**, *7*, 1902315.
- [10] N. N. Nguyen, H. C. Lee, B. Kang, M. Jo, K. Cho, *Nano Lett.* **2019**, *19*, 1758.
- [11] a) Q. H. Wang, Z. Jin, K. K. Kim, A. J. Hilmer, G. L. Paulus, C. J. Shih, M. H. Ham, J. D. Sanchez-Yamagishi, K. Watanabe, T. Taniguchi, J. Kong, P. Jarillo-Herrero, M. S. Strano, *Nat. Chem.* **2012**, *4*, 724; b) J. Xue, J. Sanchez-Yamagishi, D. Bulmash, P. Jacquod, A. Deshpande, K. Watanabe, T. Taniguchi, P. Jarillo-Herrero, B. J. LeRoy, *Nat. Mater.* **2011**, *10*, 282.
- [12] O. M. Roscioni, L. Muccioli, A. Mityashin, J. Cornil, C. Zannoni, *J. Phys. Chem. C* **2016**, *120*, 14652.
- [13] W. Gao, R. Huang, *J. Phys. D: Appl. Phys.* **2011**, *44*, 452001.
- [14] a) A. Venugopal, J. Chan, X. Li, C. W. Magnuson, W. P. Kirk, L. Colombo, R. S. Ruoff, E. M. Vogel, *J. Appl. Phys.* **2011**, *109*, 104511; b) E. Lee, H. C. Lee, S. B. Jo, H. Lee, N.-S. Lee, C. G. Park, S. K. Lee, H. H. Kim, H. Bong, K. Cho, *Adv. Funct. Mater.* **2016**, *26*, 562.
- [15] a) S. Vangala, G. Siegel, T. Prusnick, M. Snure, *Sci. Rep.* **2018**, *8*, 8842; b) S. M. Kim, A. Hsu, M. H. Park, S. H. Chae, S. J. Yun, J. S. Lee, D.-H. Cho, W. Fang, C. Lee, T. Palacios, M. Dresselhaus, K. K. Kim, Y. H. Lee, J. Kong, *Nat. Commun.* **2015**, *6*, 8662.
- [16] C. Ojeda-Aristizabal, E. J. G. Santos, S. Onishi, A. Yan, H. I. Rasool, S. Kahn, Y. Lv, D. W. Latzke, J. Velasco, Jr., M. F. Crommie, M. Sorensen, K. Gotlieb, C. Y. Lin, K. Watanabe, T. Taniguchi, A. Lanzara, A. Zettl, *ACS Nano* **2017**, *11*, 4686.
- [17] K. Kim, T. H. Lee, E. J. G. Santos, P. S. Jo, A. Salleo, Y. Nishi, Z. Bao, *ACS Nano* **2015**, *9*, 5922.
- [18] a) P. A. Gravi, M. Devel, P. Lambin, X. Bouju, C. Girard, A. A. Lucas, *Phys. Rev. B* **1996**, *53*, 1622; b) H. Ulbricht, G. Moos, T. Hertel, *Phys. Rev. Lett.* **2003**, *90*, 095501.
- [19] a) J. A. Venables, G. D. T. Spiller, M. Hanbucken, *Rep. Prog. Phys.* **1984**, *47*, 399; b) J. A. Venables, H. Brune, *Phys. Rev. B* **2002**, *66*, 195404.
- [20] P. Järvinen, S. K. Hämmäläinen, K. Banerjee, P. Häkkinen, M. Ijäs, A. Harju, P. Liljeroth, *Nano Lett.* **2013**, *13*, 3199.
- [21] S. Bommel, N. Kleppmann, C. Weber, H. Spranger, P. Schaffer, J. Novak, S. V. Roth, F. Schreiber, S. H. Klapp, S. Kowarik, *Nat. Commun.* **2014**, *5*, 5388.
- [22] a) N. N. Nguyen, S. B. Jo, S. K. Lee, D. H. Sin, B. Kang, H. H. Kim, H. Lee, K. Cho, *Nano Lett.* **2015**, *15*, 2474; b) S. B. Jo, H. H. Kim, H. Lee, B. Kang, S. Lee, M. Sim, M. Kim, W. H. Lee, K. Cho, *ACS Nano* **2015**, *9*, 8206; c) M. A. Brady, G. M. Su, M. L. Chabinc, *Soft Matter* **2011**, *7*, 11065; d) M. Sim, J. Shin, C. Shim, M. Kim, S. B. Jo, J.-H. Kim, K. Cho, *J. Phys. Chem. C* **2014**, *118*, 760; e) R. R. Lunt, J. B. Benziger, S. R. Forrest, *Adv. Mater.* **2010**, *22*, 1233.